



# *In vivo* sensitivity estimation and imaging acceleration with rotating RF coil arrays at 7 Tesla



Mingyan Li<sup>a,\*</sup>, Jin Jin<sup>a</sup>, Zhentao Zuo<sup>b,\*</sup>, Feng Liu<sup>a</sup>, Adnan Trakic<sup>a</sup>, Ewald Weber<sup>a</sup>, Yan Zhuo<sup>b</sup>, Rong Xue<sup>b</sup>, Stuart Crozier<sup>a</sup>

<sup>a</sup>School of Information Technology and Electrical Engineering, The University of Queensland, Brisbane, QLD 4072, Australia

<sup>b</sup>State Key Laboratory of Brain and Cognitive Science, Beijing MRI Centre for Brain Research, Institute of Biophysics, Chinese Academy of Sciences, Beijing, 100101, China

## ARTICLE INFO

### Article history:

Received 8 July 2014

Revised 11 December 2014

Available online 26 December 2014

### Keywords:

Human brain imaging

*In vivo* sensitivity estimation

Rotating RF coil array (RRFCA)

Phased array coils

Parallel imaging

7 Tesla

Rotating SENSitivity Encoding (rotating-SENSE)

Signal-to-noise ratio (SNR)

## ABSTRACT

Using a new rotating SENSitivity Encoding (rotating-SENSE) algorithm, we have successfully demonstrated that the rotating radiofrequency coil array (RRFCA) was capable of achieving a significant reduction in scan time and a uniform image reconstruction for a homogeneous phantom at 7 Tesla. However, at 7 Tesla the *in vivo* sensitivity profiles ( $B_1^-$ ) become distinct at various angular positions. Therefore, sensitivity maps at other angular positions cannot be obtained by numerically rotating the acquired ones. In this work, a novel sensitivity estimation method for the RRFCA was developed and validated with human brain imaging. This method employed a library database and registration techniques to estimate coil sensitivity at an arbitrary angular position. The estimated sensitivity maps were then compared to the acquired sensitivity maps. The results indicate that the proposed method is capable of accurately estimating both magnitude and phase of sensitivity at an arbitrary angular position, which enables us to employ the rotating-SENSE algorithm to accelerate acquisition and reconstruct image. Compared to a stationary coil array with the same number of coil elements, the RRFCA was able to reconstruct images with better quality at a high reduction factor. It is hoped that the proposed rotation-dependent sensitivity estimation algorithm and the acceleration ability of the RRFCA will be particularly useful for ultra high field MRI.

© 2014 Elsevier Inc. All rights reserved.

## 1. Introduction

Reducing the scan time of magnetic resonance imaging (MRI) is important for both clinical diagnosis and scientific research. Clinically, acquiring high resolution images normally requires long scan duration, which may discomfort patients and generate motion-related artifacts that affect diagnostic accuracy. In research, especially in functional MRI (fMRI), shorter scan time facilitates improving quantification of the brain activity. The fast full  $k$ -space acquisition schemes have been developed for modern MRI systems to shorten scan time, such as echo planar imaging (EPI) [1], fast spin echo [2] and fast gradient echo imaging [3]. More recently, phased array coils (PACs) [4,5] have facilitated partial  $k$ -space acquisition to further reduce the scan time. Images can then be reconstructed with different algorithms, such as simultaneous acquisition of spatial harmonics (SMASH) [6], SENSitivity Encoding (SENSE) [7,8], generalized autocalibrating partially parallel acquisitions (GRAPPA) [9].

As an alternative method, we have introduced the rotating radiofrequency coil (RRFC) [10,11] and the rotating radiofrequency coil array (RRFCA) [12–14] to reduce scan duration by using SENSE-like reconstruction methods. Both rotating RF systems are capable of encoding  $k$ -space data with varying sensitivity profiles ( $B_1^-$ ), which benefit the signal encoding process and reconstruction algorithms. By adopting the time-division multiplexing sensitivity encoding (TDM-SENSE), the RRFC demonstrated a 2-fold scan time reduction for human brain imaging [11]. The RRFCA used the rotating-SENSE algorithm that featured time-varying sensitivity profiles for acquisition acceleration and image reconstruction. A 4-element RRFCA was prototyped and tested with a homogeneous phantom at 7 Tesla, which exhibited improved g-maps [7] and uniform signal-to-noise ratio (SNR) distributions compared with a traditional stationary 8-element coil array [12,14].

In this work, the feasibility of using the RRFCA for human brain imaging was tested. Since the rotating-SENSE algorithm needs sensitivity information for image reconstruction, in our previous studies [11,14], a small number of sensitivity maps acquired at several angular positions were numerically rotated to estimate sensitivity at other positions. This technique was used for human brain imag-

\* Corresponding authors.

E-mail addresses: [mingyan@itee.uq.edu.au](mailto:mingyan@itee.uq.edu.au) (M. Li), [ztzuo@bcsllab.ibp.ac.cn](mailto:ztzuo@bcsllab.ibp.ac.cn) (Z. Zuo).

ing at 2 Tesla [10,11] owing to the negligible coil–tissue interaction [15–19] (dielectric resonance [20–22], or constructive and destructive interference [23,24]). This approach was also used for imaging a homogeneous phantom at 7 Tesla, provided the phantom and the RRFA system are both symmetrical [14]. However, this method is not applicable for *in vivo* sensitivity estimation at 7 Tesla, because the *in vivo* sensitivity maps at different angular positions vary significantly. Since measuring sensitivity at every angular position is impractical and compromises the fast imaging purpose, a practical and robust sensitivity estimation method is needed for *in vivo* applications of the RRFA at ultra high fields.

Here we investigate a novel sensitivity estimation method specially designed for *in vivo* applications of the RRFA. Instead of simply rotating the acquired sensitivity to new angular positions, the *in vivo* sensitivity maps will be deformed in a non-linear fashion. These deformations can be calculated with image registration techniques by registering *in vivo* sensitivity to sensitivity in the library which was acquired from scans of volunteers or numerical calculations. This approach is based on the observation that the  $B_1^-$  map is not particularly sensitive to small local changes, in terms of dielectric properties and structures of tissues. Instead,  $B_1^-$  maps are typically related to the global dielectric property distribution relative to the RF system [24–26], with lower spatial frequencies. This sensitivity deformation can be modelled numerically using image registration techniques [27–29], as these techniques are commonly used in finding the spatial correspondence between two images. Importantly, image registration has recently found application in modelling the magnetic field variations due to changes in dielectric distributions between different subjects [30].

In this work, the proposed numerical method will be applied to estimate the rotated sensitivity maps, which will then be used to optimise the rotating technique and reconstruct the images. The optimisation of the rotating scheme is achieved by minimising the maximum  $g$ -factor, which suppresses the noise amplification in the imaging acceleration. The  $g$ -maps, reconstructed images and SNR maps of the RRFA and stationary coil array will then be compared.

## 2. Methods and materials

As described in previous work [14], the RRFA moves to various angular positions during acquisition, so that different  $k$ -space phase-encoding lines are associated with distinct coil sensitivity profiles which improve encoding capability. In order to reduce the overall scan time, sensitivity maps at most angular positions are estimated from a small number of measured *in vivo* sensitivity maps, by employing the proposed algorithm. The linear superposition of individual sensitivity maps with global coverage of the sample can benefit the registration algorithm [31] (details are discussed in later sections). However, four physical elements with  $90^\circ$  intervals of the RRFA prototype are insufficient to provide a complete coverage. Consequently, two sets of sensitivity maps, with angular separation of  $45^\circ$  (e.g. position 1:  $0^\circ + 45^\circ$  in Fig. 1), are used together to simulate a rotating array with 8 elements equidistantly distributed in angular direction. Considering that all elements are identical, the range of angular displacement that the RRFA needs to travel is from  $-22.5^\circ$  to  $+22.5^\circ$ . In order to test the robustness of the estimation algorithm at the maximum angular rotation, sensitivity with  $22^\circ$  displacement (position 3) from position 1 is estimated. In addition, the intermediate angular position displacement ( $10^\circ$  at position 2) is also estimated. (as shown in Fig. 1, estimate  $B_1^-$  at positions 2 and 3 from acquired  $B_1^-$  at position 1). To verify the robustness of the proposed algorithm, two volunteers of different genders and distinctly different head sizes were imaged.

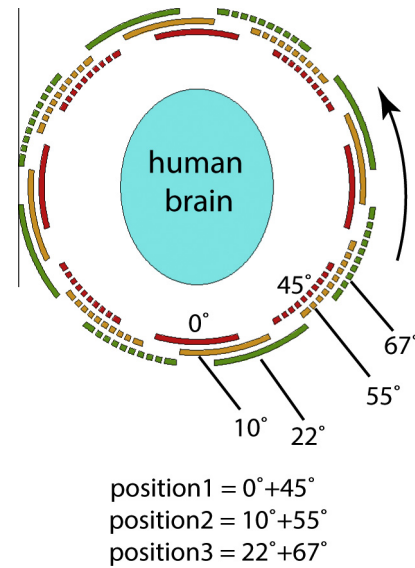


**Fig. 1.** The sensitivity profiles of the 4-element RRFA were acquired at angular positions at  $0^\circ$ ,  $10^\circ$ ,  $22^\circ$ ,  $45^\circ$ ,  $55^\circ$  and  $67^\circ$ , denoted with red, yellow, green, dashed red, dashed yellow and dashed green. Sensitivity maps acquired at these positions were recombined as three positions for better registration performance: position 1 ( $0^\circ + 45^\circ$ ), position 2 ( $10^\circ + 55^\circ$ ), position 3 ( $22^\circ + 67^\circ$ ). (For interpretation of the references to color in this figure legend, the reader is referred to the web version of this article.)

### 2.1. Registration based *in vivo* sensitivity estimation

In this work, the new sensitivity estimation method uses the acquired sensitivity at the initial position to estimate the sensitivity at other positions by employing a sensitivity library and registration techniques. The library provides source images, which are made up of sensitivity maps at all angular positions acquired during scans of volunteers. The registration techniques are employed to find the spatial transformation that aligns the source image (library sensitivity) to the target image (actual acquired sensitivity) from its initial position, and this transformation is applied to other angular positions for estimating corresponding sensitivity maps. The rotational sensitivity at arbitrary angular positions is acquired by following four steps:

- (1) Create a library by acquiring sensitivity maps at all angular positions from the scans of the volunteers. During the actual patient scanning, sensitivity maps at an initial position (i.e., position 1 in Fig. 1) are acquired. Image processing is applied to both groups of sensitivity maps to smooth profiles and correct singular values.
- (2) Instead of registering individual coil sensitivity maps, they are linearly combined before being registered, to improve accuracy and efficiency. The combination coefficients are determined with a condition number of 1 to achieve the optimal sensitivity estimation when individual sensitivity profiles are later extracted (see Step (4)).
- (3) As illustrated using a flow chart in Fig. 2, the source profile  $\vec{S}_1^8$  (combined 8 library  $B_1^-$  maps at position 1) is registered to

the target profile  $\vec{T}_1^8$  (combined 8 *in vivo*  $B_1^-$  maps at position 1). The corresponding transformation  $\Psi_1^8$  is extracted and applied to the combined library sensitivity map at arbitrary angular position ( $\alpha^\circ$ ) to obtain the estimated combined sensitivity map  $\vec{E}_\alpha^8$ .

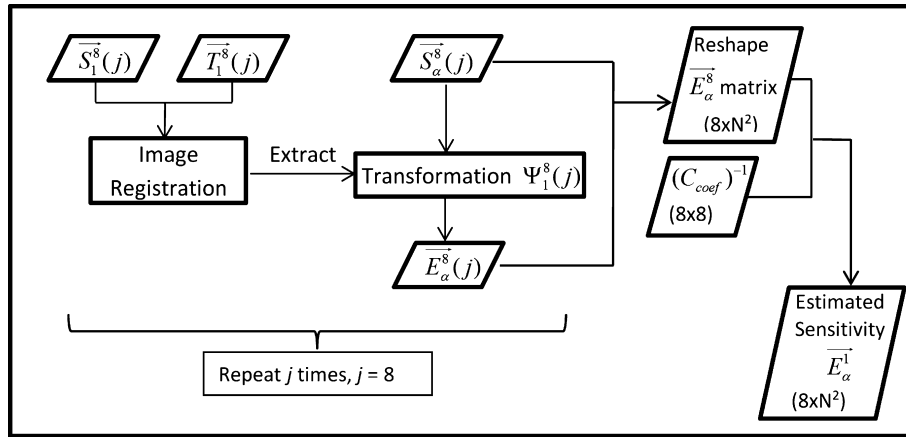


Fig. 2. Flow chart of the registration based rotation-dependent sensitivity estimation.

- (4) Repeat step (3) 8 times for all the linear combinations to estimate all the combined sensitivity maps. The individual sensitivity map  $\bar{E}_\alpha^1$  at  $\alpha^\circ$  angular position (i.e., positions 2, 3 in Fig. 1) is calculated by multiplying the inverse of the coefficient matrix.  $N^2$  in Fig. 2 denotes the number of pixels.

#### 2.1.1. In vivo sensitivity mapping and singular value correction

The most common sensitivity mapping method for a stationary coil array is to derive relative coil sensitivity by dividing the individual coil image using a predominantly uniform reference image. Both the coil image and the reference image can be obtained from either full  $k$ -space sampling [7,32] or fully sampled central  $k$ -space [33,34]. Without a uniform volume transmit coil, the reference image is typically approximated as the root sum of square (RSS) image:

$$\text{RSS} = \left| \sqrt{\sum_{j=1}^J (\bar{I}_j)^2} \right| \quad (1a)$$

$$\bar{S}_j = \frac{\bar{I}_j}{\text{RSS}} \quad (1b)$$

where  $J$  is the total number of coil elements in an array;  $\bar{I}_j$  is the full-FOV image obtained with the  $j$ -th coil;  $\bar{S}_j$  is the sensitivity map of the individual coil.

The direct division in Eq. (1b) can easily generate singular values. The different singular value distributions of each coil can cause inaccurate reconstructions which, particularly in this work, can misinform the registration process.

Singular values are commonly seen at the interfaces (i.e. skin and skull, skin and air) for both magnitude and phase of the sensitivity maps. In addition, the phase of sensitivity is often unpredictably wrapped for the ultra high field MRI. To prepare sensitivity profiles for registration, a multi-level singular value removal algorithm was developed. Similar to methods employed in [35], the map was first divided into reliable and unreliable regions. The unreliable regions consist of singular values of the magnitude map, sensitivity voids and phase discontinuities [36]. An interpolation/extrapolation procedure [35], based on polynomial fitting, was then performed to correct the sensitivity profiles in the unreliable regions.

#### 2.1.2. Optimal sensitivity combination

Due to the complex coil–tissue interactions at ultra high fields, after loading a heterogeneous subject like the human brain, the sensitivity of each coil becomes distinct [25]. For this reason, single

coil sensitivity based estimation is compromised by insufficient coil–tissue information. In addition, the registration algorithm works less efficiently with signal voids that are commonly seen in single-channel sensitivity maps. For better estimation, sensitivity profiles are linearly combined before applying registration. A similar method has been reported for optimal  $B_1$  mapping [31]. This process is expressed as:

$$C_{\text{coef}} S_{\text{single}} = S_{\text{combined}} \quad (2)$$

where  $C_{\text{coef}}$  denotes an  $8 \times 8$  coefficient matrix;  $S_{\text{single}}$  is the sensitivity matrix resized to  $8 \times N^2$  (resolution is  $N \times N$ ) and each row is a single coil sensitivity.  $S_{\text{combined}}$  contains the linearly combined sensitivity maps.

During rotating, the coil–tissue interaction is fully transformed from one angular position to another and Eq. (2) is applied accordingly. As shown in Fig. 2, to decompose the estimated individual coil sensitivity  $\bar{E}_\alpha^1$  from estimated combined sensitivity maps  $\bar{E}_\alpha^8$ , the inversion of  $C_{\text{coef}}$  is multiplied to both sides of equation. With the method described in [31], the matrix  $C_{\text{coef}}$  is determined with condition number 1 to minimise error.

#### 2.1.3. The registration technique for sensitivity estimation

The goal of registration is to find the spatial correspondence between the source and target images. Registration techniques are widely used in medical imaging [27,28,37,38], such as when information from multiple modalities are combined (computed tomography (CT), MRI, positron emission tomography (PET)), intra-subject motion correction, distortion correction, dynamic imaging reconstruction and high-field MRI safety assessment [30]. A typical registration algorithm includes two components: a similarity metric and geometric deformation. The registration algorithm employed here followed, in part, previously published works [29,39], while various components were adapted to suit the current application. For example, a similarity metric was modified to cope with complex-valued sensitivity maps.

**2.1.3.1. Similarity metric.** The similarity metric measures how well the source image aligns to the target image. Various metrics have been developed for image registration, such as squared difference (SD), mutual information (MI) [40,41] and pattern intensity (PI) [42].

Sensitivity maps are complex images. Both magnitude and phase of  $B_1^+$  and  $B_1^-$  exhibit a rotational property [25] which offers opportunities to apply image registration techniques for estimating sensitivity maps. Magnitude images are relatively easy to be registered because the features are clear; however, registering

phase images is problematic due to phase-wrapping. Even when the phase images are unwrapped, the unwrapping quality and phase ranges are difficult to control which can undermine the registration performance. To avoid this problem, the registration process in this work was not solely performed on phase images, but on the complex sensitivity maps. The PI metric was modified to cope with complex numbers. The SD metric was chosen for registering magnitude images due to its fast processing speed. Two registration processes were set to different convergence parameters for optimal performance.

For a source image  $I_s(x, y)$  and a target image  $I_t(x, y)$ , a two-dimensional SD and PI are defined as:

$$SD = \frac{\sum_{x=1}^X \sum_{y=1}^Y (I_s(x, y) - I_t(x, y))^2}{XY} \quad (3a)$$

$$PI_{r, \sigma} = \sum_{x, y} \sum_{(x-u)^2 + (y-v)^2 \leq r^2} \frac{\sigma^2}{\sigma^2 + (I_{diff}(x, y) - I_{diff}(u, v))^2} \quad (3b)$$

$$I_{diff} = I_t - I_s$$

where  $x$  and  $y$  are the voxel coordinates in the image,  $X$  and  $Y$  are the numbers of the voxels along each dimension. In Eq. (3b),  $I_{diff}$  is the difference image. The parameter  $r$  defines the size of the neighbourhood, in which the variations are taken into account. The parameter  $\sigma$  is a sensitivity controller to decide whether the variation is a structure or not.

**2.1.3.2. Geometric deformation.** Two types of geometric deformation, affine transformation and non-rigid transformation, were employed in this work. The affine transformation included translations and rotations, making it best suited for global transformations. The non-rigid transformation was applied to compensate the inefficiency of the affine transformation in local areas. In the non-rigid transformation, a deformation field recorded all displacement vectors at each voxel from an aligned source image to the target image. In this work, a free-form deformation (FFD) based on B-splines [43] was adopted for non-rigid transformations. The FFD worked by deforming a source image by manipulating a mesh of control grids [44]. To improve its efficiency, a coarse-to-fine multilevel B-spline approximation was adopted to generate a series of B-spline functions incorporating bicubic interpolation functions for calculation of the deformed pixel values.

## 2.2. Image reconstruction and encoding optimisation

The rotating coil array emulates a large amount of coils with only four physical RF elements, thereby improving the condition of the encoding matrix to facilitate a higher reduction factor. However, the encoding ability of RRFA can be further improved by strategically choosing the rotating degree for each stepping, which is determined by the  $g$ -map based optimisation algorithm [14].

### 2.2.1. Image reconstruction with rotating-SENSE

The number of sensitivity profiles limits the sensitivity encoding ability of a stationary coil array; therefore, the sensitivity profiles in the encoding matrix remain unchanged from row to row for each coil. However, the encoding matrix ( $A_R$ ) of the RRFA has more variations in its rows by taking rotational sensitivity into account:

$$A_R = \begin{bmatrix} ES_1 \\ ES_2 \\ \vdots \\ ES_4 \end{bmatrix} \quad (4)$$

where  $E = e^{iK_\kappa r_\rho}$  and  $S_j = S_j(r_\rho, t)$ .

$\kappa \in [1, M \times N/R]$ ,  $t \in [1, M/R]$ ,  $N$  is the length of a  $k$ -space line,  $M$  is the number of  $k$ -space lines and  $R$  is the reduction factor.  $E$  and  $S_j$  denote the Fourier encoding and sensitivity encoding matrices, respectively.  $K_\kappa$  denotes the  $\kappa$ -th  $k$ -space sampling position;  $r_\rho$  and  $t$  in  $S_j$  denote the sensitivity at the position of  $\rho$ -th voxel of the step  $t$ .

The Fourier encoding kernel is consistent between the stationary and rotating array; however, sensitivity maps for individual coils  $j$  at each step  $t$  are different as the coil rotates. This variation improves the condition of encoding matrix and can be exploited for further scan time reduction [14].

The noise behaviour analysis of the rotating-SENSE is similar to that of the traditional stationary array. However, to employ  $g$ -maps [7] for noise analysis, the sensitivity matrix  $S$  needs to be delineated from encoding matrix  $A_R$ :

$$A_R = FS \quad (5)$$

where  $F$  and  $S$  represent the Fourier encoding matrix and sensitivity matrix, respectively. The sensitivity matrix  $S$  consists of the

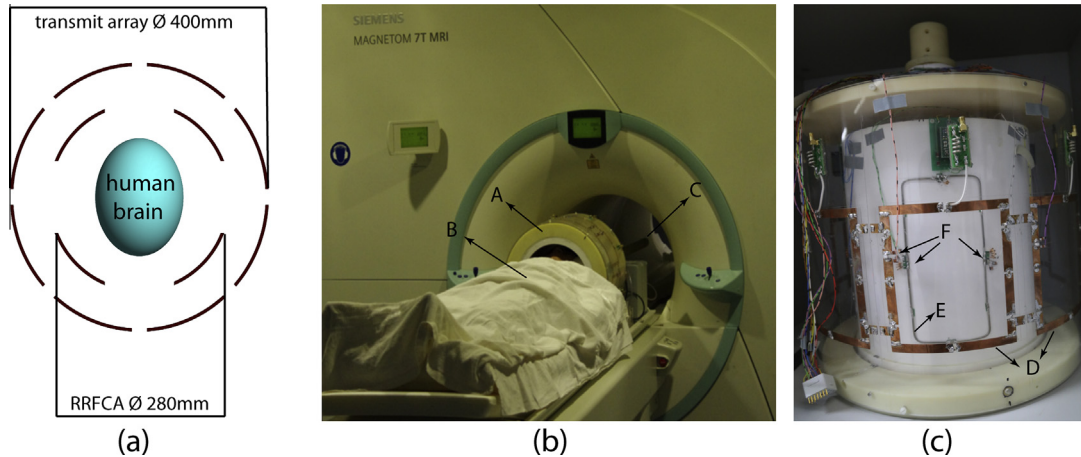


**Fig. 3.** (a) Top view of the RRFA setup. The outside layer is the stationary 8-element transmit coil array with 400 mm diameter, inner layer is the 4-element RRFA with 280 mm diameter. (b) RRFA system loaded with a volunteer. [A] RRFA system. [B] Volunteer. [C] Extended shaft pointing to rear of MRI. (c) Close-up of the RRFA system. [D] Transmit coils made of copper patches attached to outside stationary former. [E] Receive coil attached to the internal rotatable former. [F] Detuning circuits on both transmit and receive coils.



acquired sensitivity and estimated sensitivity profiles. See [14] for the process of separating  $F$  and  $S$ .

### 2.2.2. Sensitivity encoding optimisation

The proposed method of estimating *in vivo* sensitivity maps enables us to investigate the optimal rotating scheme using numerical simulations. By optimally choosing the sampling position of each step, the sensitivity encoding capability can be maximised. At each angular position, the coil sampled one phase-encoding line. The angular displacement  $\theta$  between adjacent acquisitions was determined by achieving the best imaging acceleration performance as follows:

$$\arg \min_{\theta} \left\{ \sqrt{\frac{\sum_{x=1}^M \sum_{y=1}^N (g_{xy}(\theta) - 1)^2}{M \times N}} \right\} \quad (6)$$

where  $\theta$  denotes the angular displacement between two  $k$ -space lines,  $g_{xy}(\theta)$  is the  $g$ -factor calculation [7] at voxel  $(x, y)$  in an image with  $M \times N$  pixels.

### 2.3. Experimental validation

The 4-channel RRFCFA was used to scan two subjects, A and B, at 6 angular positions ( $0^\circ$ ,  $10^\circ$ ,  $22^\circ$ ,  $45^\circ$ ,  $55^\circ$  and  $67^\circ$  in Fig. 1). These data were firstly combined to simulate an 8-channel RRFCFA (for reasons described previously). To test the proposed algorithm in an intra-subject case, images of subject A were acquired at two slices with 12 mm spacing. Sensitivity maps of one slice were used as the library. In the inter-subject case, sensitivity maps of subject A were used as the library to estimate sensitivity maps of subject B. The image registration techniques were then applied to both datasets for the estimation of the rotation-dependent sensitivity profiles at desired positions.

To study the rotating coil array in the reception mode independently without the complication from changing transmission profiles, a 4-element RRFCFA [14] was used as a receive-only coil array. An additional transmit coil array was built to provide an unchanged and relatively uniform transmission. The experimental setup is shown in Fig. 3(b) with one healthy volunteer on a whole-

body 7T MRI scanner (Magnetom 7T MRI, Siemens Medical Solutions, Erlangen, Germany). All imaging protocols were approved by institutional review board of Institute of Biophysics of Chinese Academy of Sciences (Beijing), and signed consent forms were collected. Small-flip-angle ( $FA = 30^\circ$ ) GRE images of two slices were acquired with  $TE/TR = 4/1000$  ms (in plane voxel size =  $2 \text{ mm} \times 2 \text{ mm}$ ).

The RRFCFA system consisted of three layers. The stationary inner layer was isolated from the rotating coils and provided support to a patient's head. The receive coils were attached to a rotatable middle layer and the transmit coils were attached to a stationary outer layer. The radius of the inner layer was set to 125 mm to comfortably accommodate the human head. As shown in Fig. 3(a) and (c), the transmit coil array consisted of eight loop coils, each of which was 160 mm in length and 130 mm in width. They were attached equidistantly to a coil former. A capacitance decoupling method was used to keep the coupling at a reasonably low level of  $-12 \text{ dB} \sim -14 \text{ dB}$  when loaded. To reduce the interaction and parasitic capacitance between the transmit and receive coils, besides employing active detuning circuits, a transmit coil former with a large radius should be used. However, in order to minimise the signal drop caused by the increased distance and to guarantee consistent rotation, the radius of the middle layer was set to 140 mm to provide a 15 mm separation from the inner layer. (Fig. 3(a),  $\varnothing_{\text{transmit}}$ : 400 mm,  $\varnothing_{\text{receive}}$ : 280 mm).

An extended shaft [14] was used to adjust the rotation angle outside of the MRI tunnel without repositioning the coil-subject set for acquisition at each angular (stepping) position. However, unlike the experiment setup using phantoms [14], the rotation indicator and the extended shaft were installed at the rear of the magnet bore (Fig. 3(b)) to allow enough space for the patient.

### 3. Results

Fig. 4(a) and (b) shows the gradient recalled echo (GRE) images of two slices from subject A. The GRE image of subject B (same slice location as Fig. 4(b)) is shown in Fig. 4(c). Their corresponding sensitivity maps are shown in (d)–(f). Since there is a large difference in head size and thus in global dielectric properties between

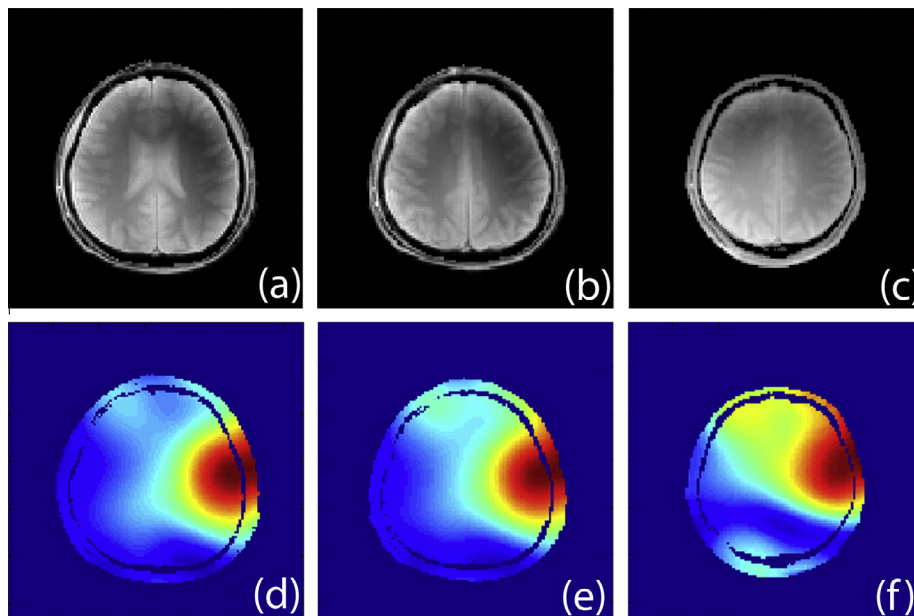


**Fig. 4.** (a) and (b) are GRE images of two slices (12 mm separation) from subject A at position 1 ( $0^\circ$ ). (c) Image from subject B of the same slice position in (b) at position 1 ( $0^\circ$ ). Their corresponding sensitivity maps are shown in (d)–(f) respectively.

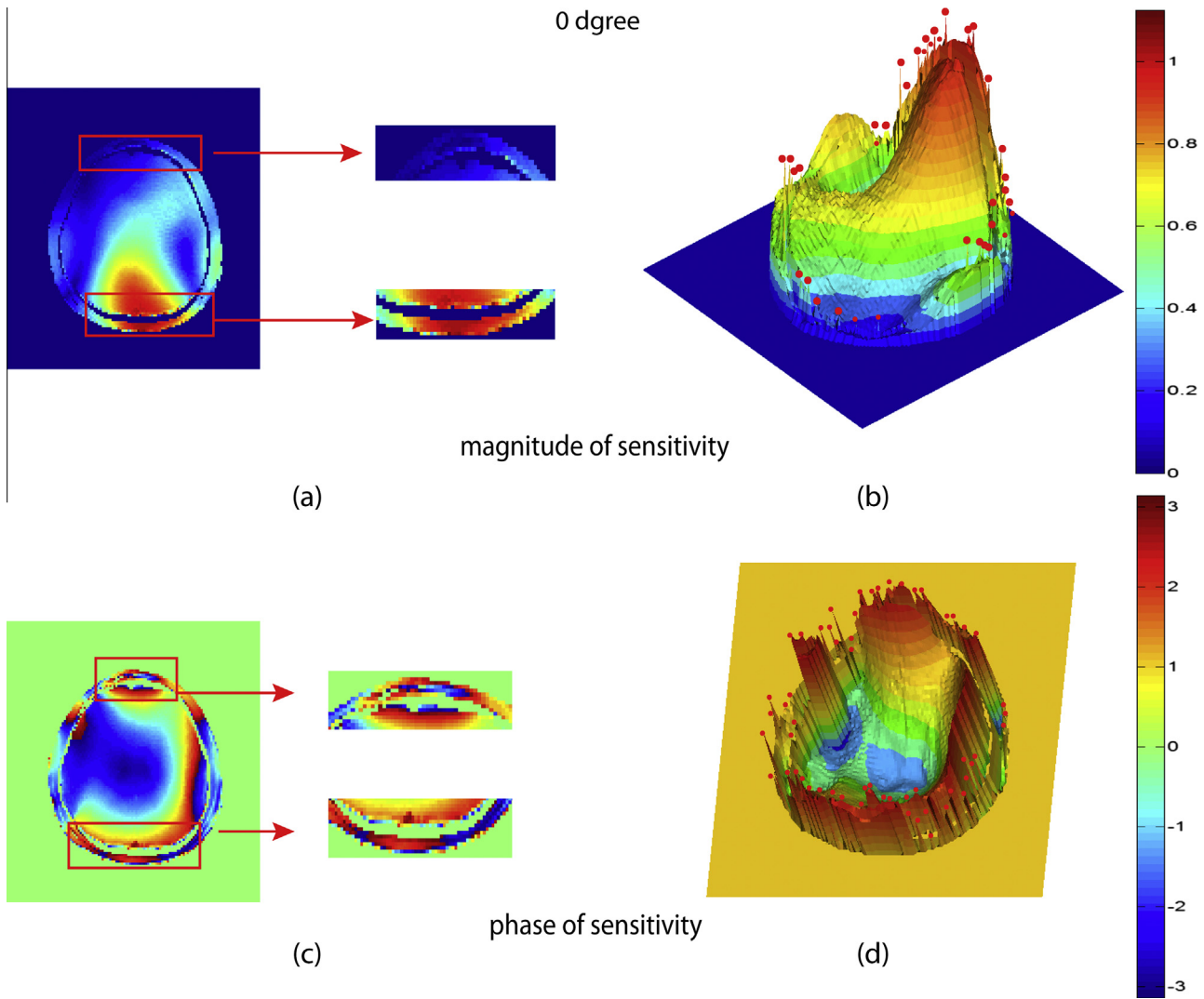


**Fig. 5.** (a) and (c) are raw magnitude and phase plots of sensitivity. The areas in the red boxes are enlarged to show singular values. In (b) and (d), the red dots denote the singular values. Compared to adjacent areas, these spikes have higher gradients and are mostly seen at the interfaces. Besides singular values, undulating errors across the raw sensitivity profiles also need to be corrected for better registration efficiency. (For interpretation of the references to color in this figure legend, the reader is referred to the web version of this article.)

subjects, large sensitivity variations are found even at the same slice location. As seen from Fig. 4(a) and (b), the anatomical structure and dielectric property of the two slices (subject A) from one subject are very different, but their sensitivity maps have minor changes shown in Fig. 4(d) and (e). This correlates with the observation that the sensitivity is more related to global dielectric changes rather than local changes.

The raw magnitude and phase maps of sensitivity derived from Eq. (1a,b) are shown in Fig. 5(a) and (c), respectively. As predicted, coil sensitivity maps should be smooth with a small local gradient. However, in Fig. 5(b) and (d), we can see that the coil sensitivity maps had abrupt changes which were associated with high gradients (marked as red dots). Magnified regions in the red boxes show the singular values. In addition, the phase map in Fig. 5(c) also exhibits the phase wrapping at the skin/air and the skull/tissue interface.

With the developed multi-level fitting algorithm, both the magnitude and phase images were smooth with the singular values corrected. In Fig. 6(a), the signal voids were also extrapolated for image registration purposes. Compared to Fig. 5(b) and (d), the high gradient and undulating errors were corrected. Both the magnitude and phase plots of sensitivity were smooth and natural.

The experimentally acquired and numerically estimated sensitivity maps for the intra-subject case are compared in Fig. 7. With a 10° angular displacement (p2 in Fig. 7(a)), the estimated magnitude maps in the second row of Fig. 7(a) were very similar to the measured sensitivity maps in the first row. Both the global features and the local details were estimated accurately. Estimated phase maps in the fourth row only showed small local variations compared to the acquired maps. Combining the magnitude and phase plots into a complex-numbered sensitivity, the root-mean-square error (RMSE) of the estimated sensitivity is 0.048. In Fig. 7(b), the angular displacement increased to 22° (position 3), which was also the largest displacement for the rotational sensitivity estimation under the current configuration. From the comparisons between the estimated and measured sensitivity maps in Fig. 7(b), we note that the minor local discrepancies started to present, although the global features of sensitivity maps were well captured by the registration based algorithm. The RMSE increased to 0.068 at p3, which suggested a slightly decreased accuracy of estimating sensitivity with a larger angular displacement.

For the inter-subject case, the experimentally acquired and numerically estimated sensitivity maps at position 2 (p2 in Fig. 8(a)) and position 3 (p3 in Fig. 8(b)) are compared in Fig. 8.

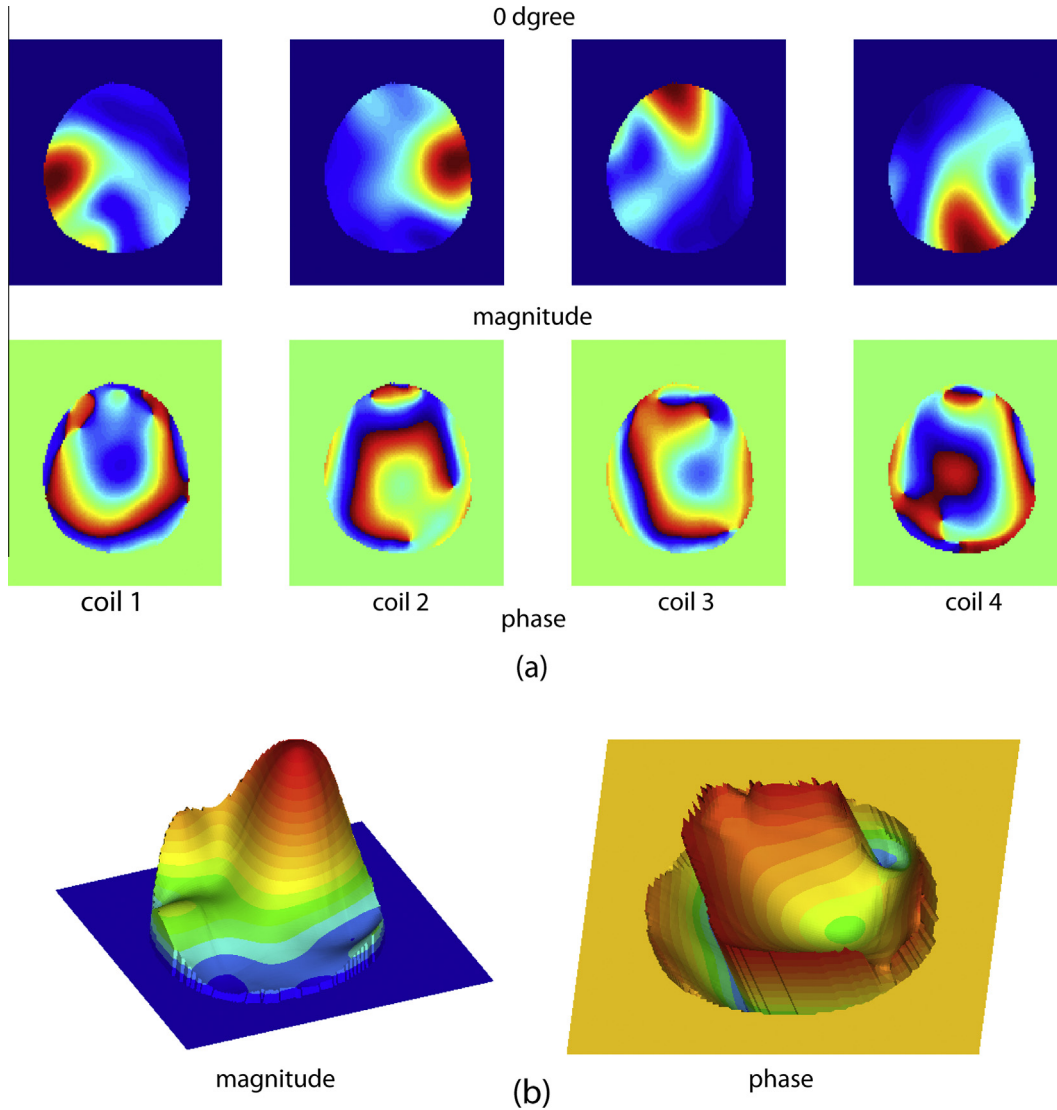


**Fig. 6.** (a) magnitude (top row) and phase (bottom row) plots of refined sensitivity map at 0°. (b) 3D magnitude (top row) and phase (bottom row) plots of refined sensitivity map for single coil.

The female subject had a noticeably smaller head than that of the male subject, therefore the sensitivity maps of two subjects have more differences compared to the intra-subject case. However, as shown in Fig. 8(a), the registration based algorithm was able to estimate the magnitude and phase maps of sensitivity accurately, both globally and locally. The RMSE was 0.054, which is slightly higher than that of the same position in the intra-subject case (RMSE = 0.048). Different from the intra-subject case, the RMSE reduced to 0.045 when the angle was then increased to 22° for position 3.

To illustrate the imaging acceleration and reconstruction ability of the RRFCAs, the  $g$ -maps, reconstructed images and the SNR maps are shown in Fig. 9 when the reduction factor was four ( $R = 4$ ). The measurements with 4-element RRFCAs sampled at two angular positions (position 1:  $0^\circ + 45^\circ$ ) were used together to emulate an 8-element stationary coil array. In the first and second rows, results reconstructed from the experimental data for 4- and 8-element stationary arrays are shown, respectively. However, the coil elements of the RRFCAs were naturally decoupled ( $-18$  dB  $S_{xy}$ ), which would be more difficult to realise with an 8-element coil array in the same size. Therefore the max  $g$ -factor in the second row may be higher than 1.7 and the averaged relative-SNR may be lower than 2.35 in practice.

Since the SNR is hard to calculate accurately for ultra high field MRI, the SNR maps in this work were calculated relative to that of a single rotating coil without undersampling ( $R = 1$ ). As we can see in Fig. 9, with a high reduction factor ( $R = 4$ ), the 4-element stationary coil array had a very high  $g$ -factor (max- $g = 3.7$ ) and a 0.95 averaged relative-SNR, which corresponded to a very noisy image with strong aliasing artifact. In contrast, under the rotating scheme of visiting 32 positions, the max  $g$ -factor (the fourth row) of 4-element RRFCAs decreased to 1.6, which was comparable to the stationary coil array with twice as many elements (max  $g = 1.7$ ) in the second row. The reconstructed image was better with lower RMSE and artifact power [45] (RMSE = 0.023, artifact power = 0.0082) compared to the 4-element stationary array (RMSE = 0.039, artifact power = 0.0231). However, fewer sensitivity profiles were available when visiting fewer angular positions, leading to higher  $g$ -factors and less capability in imaging acceleration. As shown in the third row, the maximum  $g$ -factor increased to 2.5 by only visiting six positions, and aliasing artifacts started to emerge in the reconstructed image. It is well known that the SNR is proportional to the square root of the number of channels [4,46]. To provide a fair comparison, an 8-channel RRFCAs was simulated by combining two sets of sensitivity profiles of the 4-channel RRFCAs with a  $45^\circ$  rotation. The  $g$ -map, reconstructed images



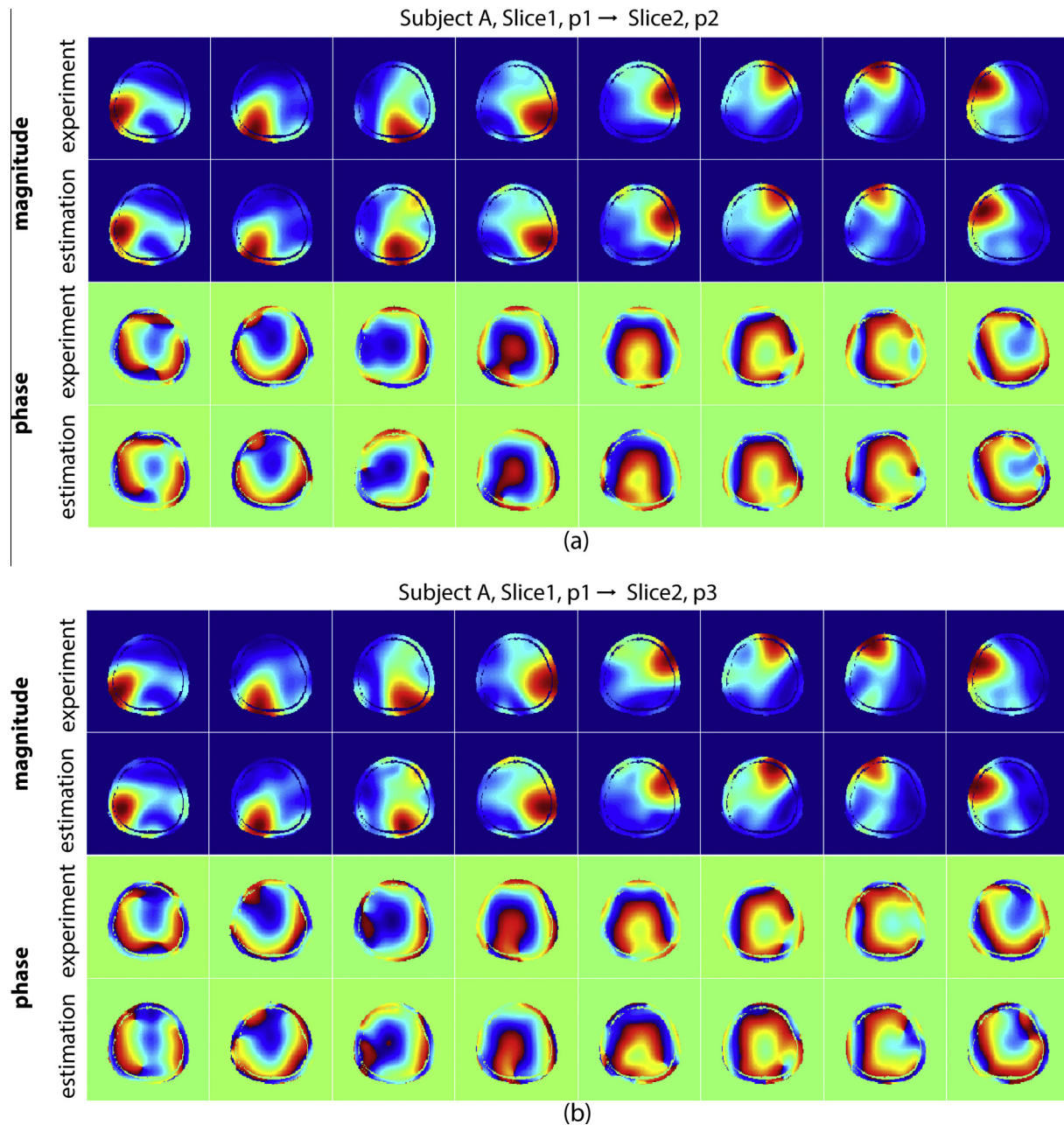


**Fig. 7.** Intra-subject case: comparisons between experimentally measured and numerically estimated sensitivity maps at position 2 (p2 in (a)) and position 3 (p3 in (b)). First row, experimentally acquired magnitude maps at p2; second row, numerically estimated magnitude maps at p2; third row: experimentally acquired phase maps at p3; fourth row, numerically estimated phase maps at p3.

and the SNR maps were shown in the fifth row for such a coil array. Compared to the second row, we can see that with the same number of coils, not only was the relative-SNR of RRFA (relative-SNR = 2.83) higher than that of the stationary array (relative-SNR = 2.35), but also the global SNR map was more uniform.

#### 4. Discussion

##### 4.1. The library data

The library data was used to provide sensitivity maps at all angular degrees, and the registration algorithm was used to bridge the discrepancy between the library and actual sensitivity maps. Theoretically, the library data can be either experimentally measured or numerically calculated. The experimentally acquired sen-

sitivity maps may be more realistic, but obtaining 3-dimensional maps at multiple positions can be time-consuming. Acquisition speed may be further restricted due to the potential heating problem for ultra high field MRI.

Commercially available electromagnetic (EM) software can be employed to calculate sensitivity maps and avoid such problems. With different algorithms, EM field distributions and related coil sensitivity can be calculated by solving Maxwell's equations. The Method of Moments (MOM) [13,18,47–50], used for calculating the EM field, is efficient for homogeneous loads, but it is not feasible to calculate heterogeneous dielectric loads due to the complexity of calculating the Green function [51]. The Finite Element Method (FEM) [52], discretising heterogeneous subjects into tetrahedral or hexahedral elements, is capable of representing complex heterogeneous subjects smoothly and providing a more accurate solution. However, the FEM requires very large computational



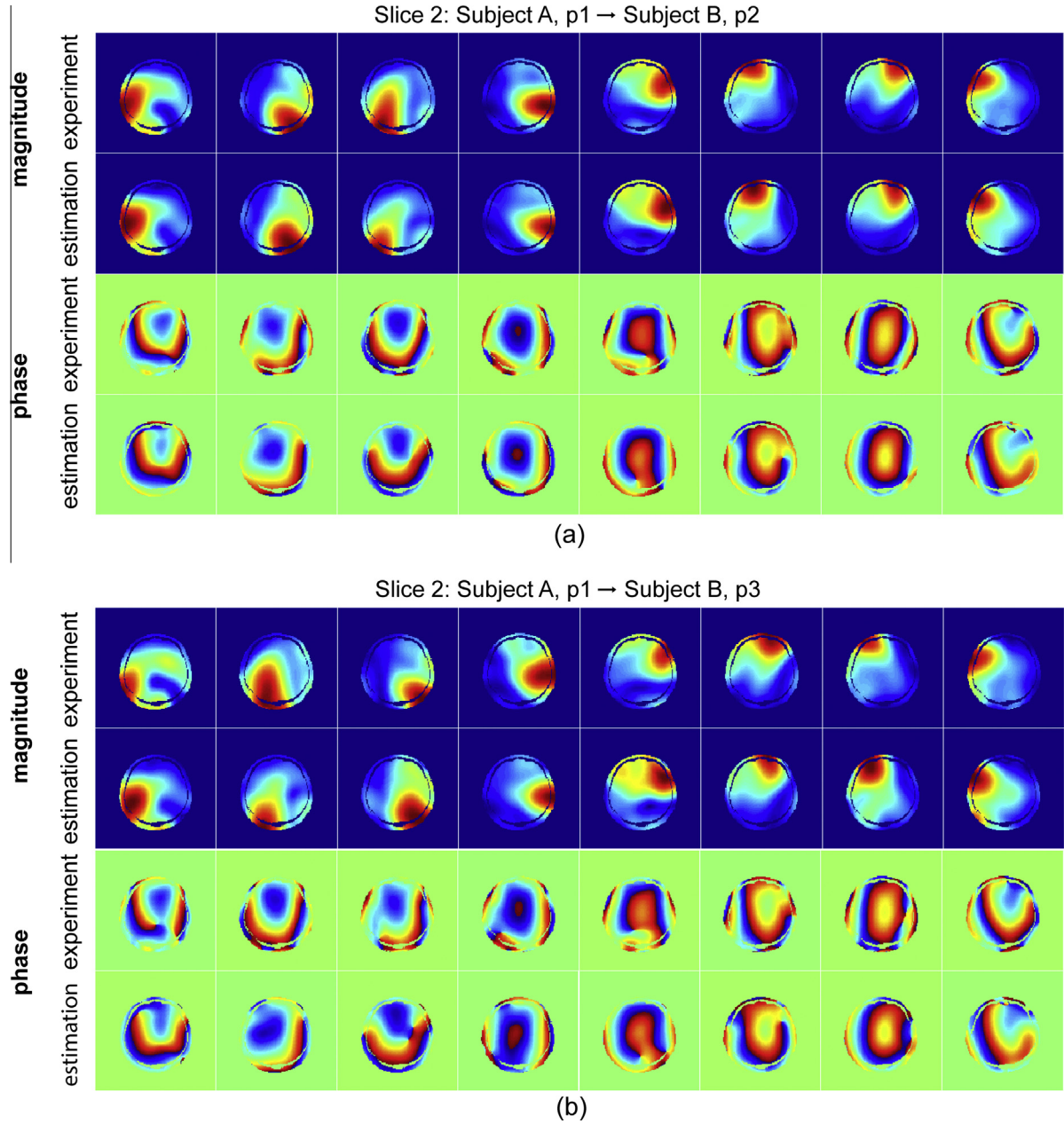


**Fig. 8.** Inter-subject case: comparisons between experimentally measured and numerically estimated sensitivity maps at position 2 (p2 in (a)) and position 3 (p3 in (b)). First row, experimentally acquired magnitude maps at p2; second row, numerically estimated magnitude maps at p2; third row: experimentally acquired phase maps at p3; fourth row, numerically estimated phase maps at p3.

resources for discretising the subjects and would have taken substantial amount of time to accurately evaluate  $B_1$ . The Finite-Difference Time-Domain (FDTD) method [53–59] has advantages over the FEM as it simplifies the discretisation into regular boxes, and the iterative solution saves on computational resources. Working in conjunction with a graphical processing unit (GPU), the calculation time can be dramatically reduced [60].

#### 4.2. Transmit $B_1^+$

A signal intensity image is determined by both transmit profile  $B_1^+$  and receive sensitivity  $B_1^-$  as illustrated in Eq. (7). At low field, the  $|B_1^+|$  is uniform and thus can be excluded from the sensitivity encoding matrix in the SENSE reconstruction. However, to include the  $|B_1^+|$  influence in the SENSE reconstruction at ultra high fields,

the actual sensitivity map in the encoding matrix should be in the form of Eq. (8) [14,61].

$$SI = M_0 |B_1^-| \sin(V\gamma\tau |B_1^+|) \quad (7)$$

$$\text{sensitivity}_{\text{actual}} = \sin(V\gamma\tau |B_1^+|_{\text{shim}}) B_1^- \quad (8)$$

where  $\gamma$  is the gyromagnetic ratio and  $M_0$  is proportional to the proton density distribution.  $\tau$  and  $V$  denotes the RF pulse duration and coil driving voltage. The asterisk denotes the complex conjugate operation.

In this work, an 8-element coil array was manufactured and actively detuned to provide an unchanged  $B_1^+$  in the course of rotation. However, the  $|B_1^+|$  inevitably changed as the array rotated, which may have introduced a small bias into the reconstruction when this changing field was not considered in the encoding

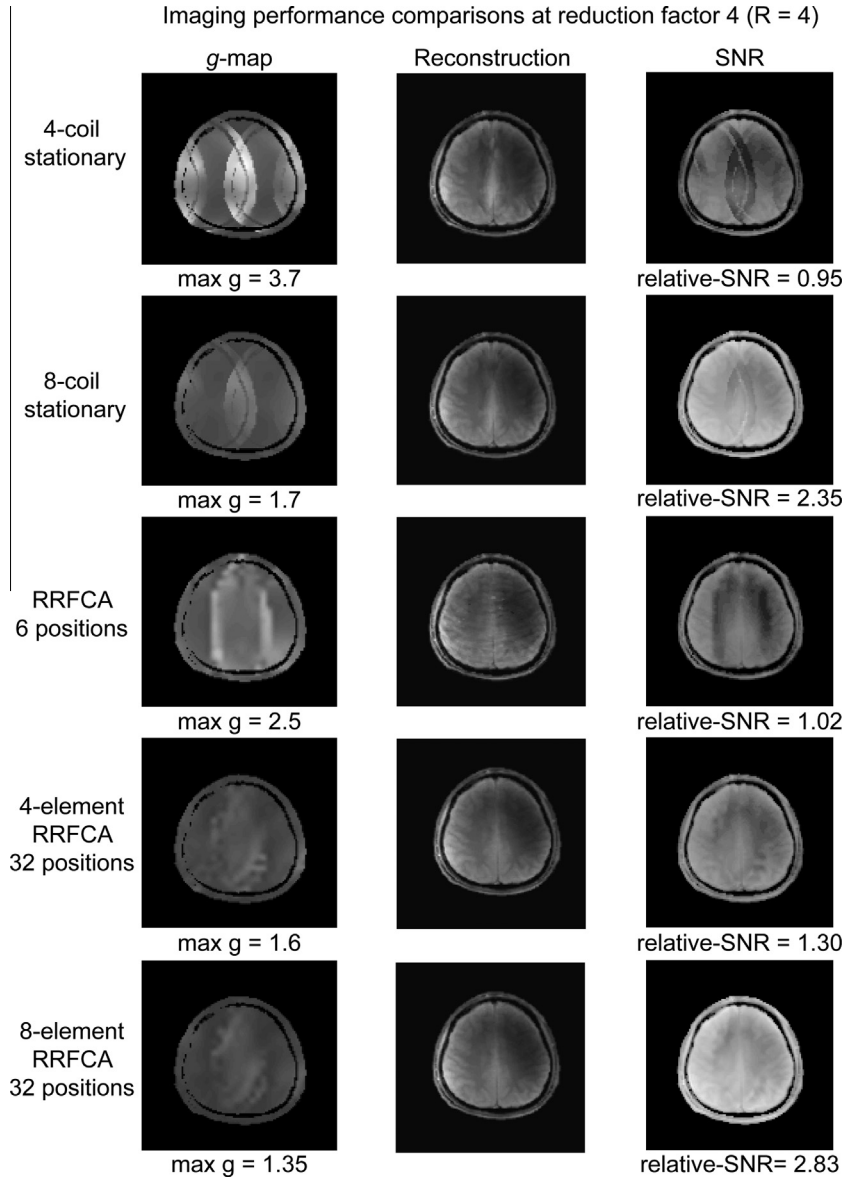


**Fig. 9.** g-map, image reconstruction and relative-SNR map comparisons between 4- and 8-element stationary coil array (first and second rows), 4-element RRFCA visiting 6 positions (third rows), 4- and 8-element RRFCA visiting 32 positions (fourth and fifth rows). Left column, g-map comparisons; middle column, image reconstruction comparisons; right column, relative-SNR map comparisons. All SNR calculations were relative to that of a single rotating coil without undersampling (SNR = 1).

matrix. To further improve the sensitivity encoding ability of the RRFCA and faithfully reconstruct the image, it may be advantageous to adopt a composite sensitivity concept [14]. Our future work will involve the development of the sensitivity estimation algorithm for the RRFCA working in transceive mode.

#### 4.3. SNR calculation

As an important metric to quantitatively evaluate image quality, the SNR calculation for MRI has been extensively studied [4,62–65]. At ultra high field ( $>3T$ ), the SNR can be expressed as [62,66]:

$$\text{SNR} = \frac{V_{\text{signal}}}{V_{\text{noise}}} \propto \frac{B_0^2 \int_{\text{VOI}} W \sin(V\gamma\tau|B_1^+|)|B_1^-|dV}{\sqrt{P_{\text{sample}}}} \quad (9)$$

where the integration is performed over the volume of interest (VOI) and  $W$  is a weighting factor related to tissue and sequence.

The  $P_{\text{sample}}$  is the power dissipated in the sample, which is too complex to be efficiently calculated for rotating array coils at ultra high fields. Thus the relative SNR was reported. In this work, to simplify the comparison, the  $P_{\text{sample}}$  for different arrays were considered the same [67], since transmission power remained approximately the same for different arrays.

In parallel imaging, the reduced  $k$ -space data are recovered by employing the coil sensitivity profiles. However, the noise is inevitably amplified in the reconstruction process, especially with a high reduction factor. The SNR calculation when employing parallel imaging algorithms, such as SENSE, can be calculated as below [7], provided that the channel number does not change:

$$\frac{\text{SNR}_{\text{PI}}}{\text{SNR}_{\text{full}}} = \frac{1}{g\sqrt{R}} \quad (10)$$

where  $g$  and  $R$  denotes the g-map and reduction factor, respectively. The SNR is also proportional to the square root of the number of channels [4,46]. In order to provide a fair SNR comparison, we

simulated the 8-channel RRFCAs by combining data obtained with a 45° separation.

#### 4.4. RRFCAs structure and data sampling

##### 4.4.1. Coil geometry

Using a large number of RF coils can increase the SNR and significantly accelerate the imaging process [68–71]. However, placing a large number of coils in a constrained space will decrease the coil size, leading to a shallower  $B_1$  penetration. Namely, smaller coils receive less signal from the centre compared to larger coils. In addition, a coil array with higher density can increase the difficulty of decoupling. Coil coupling undermines the parallel imaging performance and reduces the SNR. By employing the rotating scheme, the RRFCAs not only provides a large number of sensitivity profiles without additional RF channels, but also allows bigger coils to be used with less decoupling complexity.

##### 4.4.2. Data sampling

The RRFCAs is designed to sample one  $k$ -space line at each stepping position, and then move to the next angular position for the following sampling. In this preliminary *in vivo* study, the stepping angle was manually adjusted and a full  $k$ -space matrix was sampled at each angular position. The accelerated acquisition was numerically modelled by extracting and combining the corresponding  $k$ -space lines.

##### 4.4.3. Rotating speed and acoustic noise

In this proof-of-concept work, the RRFCAs was manually rotated to sample data at several angular positions in order to validate the proposed *in vivo* sensitivity estimation algorithm. In our previous works [10,11], the rotating coil was pneumatically driven to achieve up to 870 rpm for human head imaging with negligible acoustic noise, compared with noise generated by the gradient system. For animal imaging, the rotating speed can easily exceed 10,000 rpm. Our recent experiments on a 9.4T pre-clinical system have shown that the rotating coil can faithfully reconstruct the images at speeds of, or exceeding, 5500 rpm.

## 5. Conclusion

In this paper, an *in vivo* rotational sensitivity estimation algorithm for the RRFCAs was proposed and verified using human head imaging. By taking advantage of registration techniques and a library data, the algorithm was able to estimate sensitivity maps with arbitrary angular displacement. The estimated sensitivity maps were then fed into the rotating-SENSE algorithm to improve the imaging acceleration ability of the 4-element RRFCAs. The 4-channel RRFCAs outperformed the 4-element stationary array and was comparable to 8-element stationary PACs in terms of  $g$ -map and reconstruction quality. The 8-element RRFCAs has been shown to significantly improve image quality compared to a stationary 8-element coil array. In the future, a sensitivity estimation algorithm for a transceive RRFCAs with “composite sensitivity” will be developed. By taking  $B_1^+$  into account in sensitivity encoding, the imaging acceleration ability of the RRFCAs can be further improved. Additionally, an automatic rotation control system for the RRFCAs will be developed by means of, for example, a non-magnetic piezo-electric or ceramic motor.

## Acknowledgments

This work was supported by Australian Research Council, the Ministry of Science and Technology of China Grant (2012CB825500), the Chinese National Major Scientific Equipment

R&D Project (Grant No. ZDYZZ2010-2), the National Nature Science Foundation of China Grant (91132302) and the Chinese Academy of Sciences Grants (XDB02010001 and XDB02050001).

## References

- [1] P. Mansfield, Multi-planar image formation using NMR spin echoes, *J. Phys. C: Solid State Phys.* 10 (1977) L55.
- [2] J. Listerud, S. Einstein, E. Outwater, H.Y. Kressel, First principles of fast spin echo, *Magn. Reson. Q.* 8 (1992) 199–244.
- [3] P. van der Meulen, J.P. Groen, J.J. Cuppen, Very fast MR imaging by field echoes and small angle excitation, *Magn. Reson. Imaging* 3 (1985) 297–299.
- [4] P.B. Roemer, W.A. Edelstein, C.E. Hayes, S.P. Souza, O.M. Mueller, The NMR phased array, *Magn. Reson. Med.* 16 (1990) 192–225.
- [5] S.M. Wright, L.L. Wald, Theory and application of array coils in MR spectroscopy, *NMR Biomed.* 10 (1997) 394–410.
- [6] D.K. Sodickson, W.J. Manning, Simultaneous acquisition of spatial harmonics (SMASH): fast imaging with radiofrequency coil arrays, *Magn. Reson. Med.* 38 (1997) 591–603.
- [7] K.P. Pruessmann, M. Weiger, M.B. Scheidegger, P. Boesiger, SENSE: sensitivity encoding for fast MRI, *Magn. Reson. Med.* 42 (1999) 952–962.
- [8] K.P. Pruessmann, M. Weiger, P. Bornert, P. Boesiger, Advances in sensitivity encoding with arbitrary  $k$ -space trajectories, *Magn. Reson. Med.* 46 (2001) 638–651.
- [9] M.A. Griswold, P.M. Jakob, R.M. Heidemann, M. Nittka, V. Jellus, J. Wang, et al., Generalized autocalibrating partially parallel acquisitions (GRAPPA), *Magn. Reson. Med.* 47 (2002) 1202–1210.
- [10] A. Trakic, B.K. Li, E. Weber, H. Wang, S. Wilson, S. Crozier, A rapidly rotating RF coil for MRI, *Concepts Magn. Reson. Part B: Magn. Reson. Eng.* 35B (2009) 59–66.
- [11] A. Trakic, H. Wang, E. Weber, B.K. Li, M. Poole, F. Liu, et al., Image reconstructions with the rotating RF coil, *J. Magn. Reson.* 201 (2009) 186–198.
- [12] M. Li, Jin Jin, Feng Liu, Ewald Weber, Adnan Trakic, Stuart Crozier, Highly accelerated parallel MRI using rotating radiofrequency coil array at 7T, in: 21st Annual Meeting and Exhibition of ISMRM, Salt Lake City, Utah, USA, 2013.
- [13] M. Li, J. Jin, A. Trakic, F. Liu, E. Weber, Y. Li, et al., High acceleration with rotating radiofrequency coil array (RRFCAs) in parallel magnetic resonance imaging (MRI), in: Presented at the 34th Annual International Conference of the IEEE Engineering in Medicine and Biology Society (EMBC'12), San Diego, 2012.
- [14] M. Li, Z. Zuo, J. Jin, R. Xue, A. Trakic, E. Weber, et al., Highly accelerated acquisition and homogeneous image reconstruction with rotating RF coil array at 7T – A phantom based study, *J. Magn. Reson.* 240 (2014) 102–112.
- [15] S. Crozier, I.M. Brereton, F.O. Zelaya, W.U. Roffmann, D.M. Doddrell, Sample-induced RF perturbations in high-field, high-resolution NMR spectroscopy, *J. Magn. Reson.* 126 (1997) 39–47.
- [16] P.S. Tofts, Standing wave in uniform water phantoms, *J. Magn. Reson.* 104 (B) (1994) 143–147.
- [17] F. Liu, S. Crozier, Electromagnetic fields inside a lossy, multilayered spherical head phantom excited by MRI coils: models and methods, *Phys. Med. Biol.* 49 (2004) 1835–1851.
- [18] F. Liu, B.L. Beck, B. Xu, J.R. Fitzsimmons, S.J. Blackband, S. Crozier, Numerical modeling of 11.1T MRI of a human head using a MoM/FDTD method, *Concepts Magn. Reson. Part B: Magn. Reson. Eng.* 24B (2005) 28–38.
- [19] G. McLaughlin, T. Ji, D. Napolitano, Material probing method for medical application, involves receiving echoes generated by interactions between ultrasound beam and material, and converting received echoes to generate echolocation data, United States Patent US2004147841-A1, 2004.
- [20] L.B. Pierre-Marie, Robitaille, Ultra High Field Magnetic Resonance Imaging, Springer Science + Business, Media, New York, USA, 2006.
- [21] T.S. Ibrahim, R. Lee, A.M. Abduljalil, B.A. Baertlein, P.M. Robitaille, Dielectric resonances and B(1) field inhomogeneity in UHFMR: computational analysis and experimental findings, *Magn. Reson. Imaging* 19 (2001) 219–226.
- [22] A. Kangarlu, B.A. Baertlein, R. Lee, T. Ibrahim, L. Yang, A.M. Abduljalil, et al., Dielectric resonance phenomena in ultra high field MRI, *J. Comput. Assist. Tomogr.* 23 (1999) 821–831.
- [23] C.M. Collins, W. Liu, W. Schreiber, Q.X. Yang, M.B. Smith, Central brightening due to constructive interference with, without, and despite dielectric resonance, *J. Magn. Reson. Imaging* 21 (2005) 192–196.
- [24] Q.X. Yang, J. Wang, X. Zhang, C.M. Collins, M.B. Smith, H. Liu, et al., Analysis of wave behavior in lossy dielectric samples at high field, *Magn. Reson. Med.* 47 (2002) 982–989.
- [25] P.F. Van de Moortele, C. Akgun, G. Adriany, S. Moeller, J. Ritter, C.M. Collins, et al., B(1) destructive interferences and spatial phase patterns at 7T with a head transceiver array coil, *Magn. Reson. Med.* 54 (2005) 1503–1518.
- [26] T.S. Ibrahim, R. Lee, B.A. Baertlein, A.M. Abduljalil, H. Zhu, P.M.L. Robitaille, Effect of RF coil excitation on field inhomogeneity at ultra high fields: a field optimized TEM resonator, *Magn. Reson. Imaging* 19 (2001) 1339–1347.
- [27] D.L. Hill, P.G. Batchelor, M. Holden, D.J. Hawkes, Medical image registration, *Phys. Med. Biol.* 46 (2001) R1–R45.
- [28] M. Holden, A review of geometric transformations for nonrigid body registration, *IEEE Trans. Med. Imaging* 27 (2008) 111–128.

- [29] D. Rueckert, L.I. Sonoda, C. Hayes, D.L. Hill, M.O. Leach, D.J. Hawkes, Nonrigid registration using free-form deformations: application to breast MR images, *IEEE Trans. Med. Imaging* 18 (1999) 712–721.
- [30] J. Jin, F. Liu, E. Weber, S. Crozier, Improving SAR estimations in MRI using subject-specific models, *Phys. Med. Biol.* 57 (2012) 8153–8171.
- [31] S.J. Malik, D.J. Larkman, J.V. Hajnal, Optimal linear combinations of array elements for B1 mapping, *Magn. Reson. Med.* 62 (2009) 902–909.
- [32] L. Ying, J. Sheng, Joint image reconstruction and sensitivity estimation in SENSE (JSENSE), *Magn. Reson. Med.* 57 (2007) 1196–1202.
- [33] C.A. McKenzie, E.N. Yeh, M.A. Ohliger, M.D. Price, D.K. Sodickson, Self-calibrating parallel imaging with automatic coil sensitivity extraction, *Magn. Reson. Med.* 47 (2002) 529–538.
- [34] F. Huang, Y. Chen, W. Yin, W. Lin, X. Ye, W. Guo, et al., A rapid and robust numerical algorithm for sensitivity encoding with sparsity constraints: self-feeding sparse SENSE, *Magn. Reson. Med.* 64 (2010) 1078–1088.
- [35] J. Jin, F. Liu, E. Weber, Y. Li, S. Crozier, An electromagnetic reverse method of coil sensitivity mapping for parallel MRI – theoretical framework, *J. Magn. Reson.* 207 (2010) 59–68.
- [36] M.D.P. Dennis, C. Ghiglia, Two-Dimensional Phase Unwrapping: Theory, Algorithms, and Software, John Wiley and Sons Inc., 1998.
- [37] J.B. Maintz, M.A. Viergever, A survey of medical image registration, *Med. Image Anal.* 2 (1998) 1–36.
- [38] R. Wan, M. Li, An overview of medical image registration, in: Fifth International Conference on Computational Intelligence and Multimedia Applications, ICCIMA, Proceedings, 2003, pp. 385–390.
- [39] J. Jin, F. Liu, S. Crozier, Image registration guided, sparsity constrained reconstructions for dynamic MRI, *Magn. Reson. Imaging* 32 (2014) 1403–1417.
- [40] F. Maes, A. Collignon, D. Vandermeulen, G. Marchal, P. Suetens, Multimodality image registration by maximization of mutual information, *IEEE Trans. Med. Imaging* 16 (1997) 187–198.
- [41] J.P.W. Pluim, J.B.A. Maintz, M.A. Viergever, Mutual-information-based registration of medical images: a survey, *IEEE Trans. Med. Imaging* 22 (2003) 986–1004.
- [42] T.M.B.J. Weese, C. Lorenz, C. Fassnacht, An approach to 2D/3D registration of a vertebra in 2D X-ray fluoroscopy, *CVRMed/MRCAS* (1997) 119–128.
- [43] D. Rueckert, P. Aljabar, R.A. Heckemann, J.V. Hajnal, A. Hammers, Diffeomorphic registration using B-splines, *Med. Image Comput. Comput. Assist. Interv.* 9 (2006) 702–709.
- [44] L. Seungyong, G. Wolberg, S. Sung-Yong, Scattered data interpolation with multilevel B-splines, *IEEE Trans. Visual. Comput. Graphics* 3 (1997) 228–244.
- [45] C.A. McKenzie, E.N. Yeh, D.K. Sodickson, Improved spatial harmonic selection for SMASH image reconstructions, *Magn. Reson. Med.* 46 (2001) 831–836.
- [46] D. Liang, H.T. Hui, T.S. Yeo, Increasing the signal-to-noise ratio by using vertically stacked phased array coils for low-field magnetic resonance imaging, *IEEE Trans. Inf. Technol. Biomed.* 16 (2012) 1150–1156.
- [47] R.F. Harrington, *Field Computation by Moment Methods*, John Wiley and Sons, New York, 1996.
- [48] H. Ochi, E. Yamamoto, K. Sawaya, S. Adachi, Analysis of a magnetic-resonance-imaging antenna inside an RF shield, *Electron. Commun. Jpn. Part I-Commun.* 77 (1994) 37–45.
- [49] S. Wright, M. Lee, Full-wave moment of method analysis of RF coils on lossy media, in: Proceeding of the 6th Annual Meeting of 10th ISMRM, San Francisco, USA, 1991.
- [50] J. Jin, F. Liu, E. Weber, Y. Li, S. Crozier, An electromagnetic reverse method of coil sensitivity mapping for parallel MRI – theoretical framework, *J. Magn. Reson.* 207 (2010) 59–68.
- [51] B.K. Li, F. Liu, E. Weber, S. Crozier, Hybrid numerical techniques for the modelling of radiofrequency coils in MRI, *NMR Biomed.* 22 (2009) 937–951.
- [52] J.M. Jin, J. Chen, On the SAR and field inhomogeneity of birdcage coils loaded with the human head, *Magn. Reson. Med.* 38 (1997) 953–963.
- [53] K. Yee, Numerical solution of initial boundary value problems involving Maxwell's equations in isotropic media, *IEEE Trans. Antennas Propagation* 14 (1966) 302–307.
- [54] K. Ugurbil, M. Garwood, J. Ellermann, K. Hendrich, R. Hinke, X.P. Hu, et al., Imaging at high magnetic-fields – initial experiences at 4-T, *Magn. Reson. Q.* 9 (1993) 259–277.
- [55] C.M. Collins, M.B. Smith, Signal-to-noise ratio and absorbed power as functions of main magnetic field strength, and definition of “90 degrees” RF pulse for the head in the birdcage coil, *Magn. Reson. Med.* 45 (2001) 684–691.
- [56] T.S. Ibrahim, A numerical analysis of radio-frequency power requirements in magnetic resonance imaging experiment, *IEEE Trans. Microwave Theory Tech.* 52 (2004) 1999–2003.
- [57] F. Liu, S. Crozier, An FDTD model for calculation of gradient-induced eddy currents in MRI system, *IEEE Trans. Appl. Supercond.* 14 (3) (2004) 1983–1989.
- [58] F. Liu, S. Crozier, H. Zhao, B. Lawrence, Finite-difference time-domain-based studies of MRI pulsed field gradient-induced eddy currents inside the human body, *Concepts Magn. Reson.* 15 (2002) 26–36.
- [59] A. Trakic, J. Jin, M.Y. Li, D. McClymont, E. Weber, F. Liu, et al., A comparative numerical study of rotating and stationary RF coils in terms of flip angle and specific absorption rate for 7T MRI, *J. Magn. Reson.* 236 (2013) 70–82.
- [60] J. Chi, F. Liu, E. Weber, Y. Li, C. Stuart, GPU-accelerated FDTD modeling of radio-frequency field–tissue interactions in high-field MRI, *IEEE Trans. Biomed. Eng.* 58 (2011) 1789–1796.
- [61] C.M. Collins, Q.X. Yang, J.H. Wang, X. Zhang, H. Liu, S. Michaeli, et al., Different excitation and reception distributions with a single-loop transmit-receive surface coil near a head-sized spherical phantom at 300 MHz, *Magn. Reson. Med.* 47 (2002) 1026–1028.
- [62] C.M. Collins, M.B. Smith, Signal-to-noise ratio and absorbed power as functions of main magnetic field strength, and definition of “90°” RF pulse for the head in the birdcage coil, *Magn. Reson. Med.* 45 (2001) 684–691.
- [63] W.A. Edelstein, G.H. Glover, C.J. Hardy, R.W. Redington, The intrinsic signal-to-noise ratio in NMR imaging, *Magn. Reson. Med.* 3 (1986) 604–618.
- [64] D.I. Hoult, R.E. Richards, The signal-to-noise ratio of the nuclear magnetic resonance experiment, *J. Magn. Reson.* (1969) 24 (1976) 71–85.
- [65] J.T. Vaughan, M. Garwood, C.M. Collins, W. Liu, L. Delabarre, G. Adriany, et al., 7T vs. 4T: RF power, homogeneity, and signal-to-noise comparison in head images, *Magn. Reson. Med.* 46 (2001) 24–30.
- [66] D.I. Hoult, D. Phil, Sensitivity and power deposition in a high-field imaging experiment, *J. Magn. Reson. Imaging* 12 (2000) 46–67.
- [67] A. Trakic, J. Jin, M.Y. Li, D. McClymont, E. Weber, F. Liu, et al., A comparative numerical study of rotating and stationary RF coils in terms of flip angle and specific absorption rate for 7T MRI, *J. Magn. Reson.* 236 (2013) 70–82.
- [68] G.C. Wiggins, J.R. Polimeni, A. Potthast, M. Schmitt, V. Alagappan, L.L. Wald, 96-Channel receive-only head coil for 3 Tesla: design optimization and evaluation, *Magn. Reson. Med.* 62 (2009) 754–762.
- [69] M. Schmitt, A. Potthast, D.E. Sosnovik, J.R. Polimeni, G.C. Wiggins, C. Triantafyllou, et al., A 128-channel receive-only cardiac coil for highly accelerated cardiac MRI at 3 Tesla, *Magn. Reson. Med.* 59 (2008) 1431–1439.
- [70] C.J. Hardy, R.O. Giaquinto, J.E. Piel, K.W. Rohling, L. Marinelli, D.J. Blezek, et al., 128-Channel body MRI with a flexible high-density receiver-coil array, *J. Magn. Reson. Imaging* 28 (2008) 1219–1225.
- [71] G.C. Wiggins, C. Triantafyllou, A. Potthast, A. Reykowski, M. Nittka, L.L. Wald, 32-Channel 3 Tesla receive-only phased-array head coil with soccer-ball element geometry, *Magn. Reson. Med.* 56 (2006) 216–223.